

An experimental simulation of oxygen isotope exchange reaction between amorphous silicate dust and carbon monoxide gas in the early Solar System

Yamamoto, Daiki
Department of Earth and Planetary Sciences, Kyushu University

Kawasaki, Noriyuki
Department of Natural History Sciences, Hokkaido University

Tachibana, Shogo
UTokyo Organization for Planetary Space Science, The University of Tokyo

Ishizaki, Lily
Department of Earth and Planetary Science, The University of Tokyo

他

<https://hdl.handle.net/2324/7178666>

出版情報 : *Geochimica et Cosmochimica Acta*. 374, pp.93-105, 2024-06. Elsevier
バージョン :
権利関係 : © 2024 The Author(s).





An experimental simulation of oxygen isotope exchange reaction between amorphous silicate dust and carbon monoxide gas in the early Solar System

Daiki Yamamoto^{a,*}, Noriyuki Kawasaki^b, Shogo Tachibana^c, Lily Ishizaki^d, Ryosuke Sakurai^d, Hisayoshi Yurimoto^b

^a Department of Earth and Planetary Sciences, Kyushu University, Motoooka, Fukuoka 819-0395, Japan

^b Department of Natural History Sciences, Hokkaido University, Sapporo, Hokkaido 060-0810, Japan

^c UTokyo Organization for Planetary Space Science, The University of Tokyo, Hongo, Tokyo 113-0033, Japan

^d Department of Earth and Planetary Science, The University of Tokyo, Hongo, Tokyo 113-0033, Japan

ARTICLE INFO

Associate editor: Ann Nguyen

Keywords:

Oxygen isotopes
Gas–solid isotope exchange
Silicate dust
Kinetics
Carbon monoxide

ABSTRACT

The reaction mechanism and kinetics of oxygen isotope exchange between tens of nanometer-sized amorphous silicate grains with forsterite composition (amorphous forsterite) and low-pressure carbon monoxide (CO) gas (P_{CO}) of 0.05–1 Pa at 643–883 K were examined to investigate oxygen isotopic evolution in the protosolar disk that led to the mass-independent oxygen isotopic variation of planetary materials. Both CO gas supply- and diffusion-controlled isotope exchange reactions were observed. At 753–883 K and P_{CO} of 0.05–1 Pa, the supply of CO gas controls the isotope exchange reaction, and its rate is 2–3 orders of magnitude smaller than that of the H_2O supply-controlled isotope exchange reaction. The diffusion-controlled isotope exchange occurred at 643–703 K and P_{CO} of 0.3 Pa, and the reaction rate of $D \text{ (m}^2\text{/s)} = (3.1 \pm 2.3) \times 10^{-23} \exp[-41.7 \pm 9.6 \text{ (kJ mol}^{-1}) R^{-1} (1/T - 1/1200)]$ was obtained.

We found that the oxygen isotope exchange rates of amorphous forsterite with CO and H_2O gases are larger than those of gaseous isotope exchange between CO and H_2O gases at a wide range of temperatures, wherein amorphous forsterite crystallization does not precede the isotope exchange reaction of amorphous forsterite with these gases. The most sluggish isotope exchange rate between H_2O and CO in the gas phase suggests that amorphous forsterite would play a role in accelerating gaseous isotopic equilibrium through the isotope exchange of amorphous forsterite with both CO and H_2O . We found that the oxygen isotopic equilibrium between 0.1 μm -sized amorphous forsterite, CO, and H_2O would be accomplished through the isotope exchange of amorphous forsterite at temperatures as low as ~ 600 – 700 K in the dynamically accreting protosolar disk, which is significantly lower than expected for the case of gaseous isotope exchange ($> \sim 800$ K).

1. Introduction

Oxygen isotopic compositions of extraterrestrial materials have garnered considerable attention in the field of cosmochemistry since the first discovery of oxygen isotopic anomalies in Allende refractory inclusions (Clayton et al., 1973). Oxygen isotopic compositions of primitive extraterrestrial materials exhibit mass-independent isotopic variation, contrary to those of terrestrial materials that show mass-dependent isotopic variation associated with chemical and/or physical processes. This mass-independent isotopic variation is consequence of isotopic separation (evolution) of the gaseous phase through self-shielding of carbon monoxide (CO) in the protosolar molecular cloud

and/or the cold region of the protosolar disk (Yurimoto and Kuramoto, 2004; Lyons and Young, 2005). In this scenario, selective dissociation of rarer CO isotopologues (C^{17}O and C^{18}O) by ultraviolet photons results in the formation of ^{16}O -poor oxygen atoms that are eventually transformed into ^{16}O -poor water ice through oxygen-hydrogen chemical reactions on the dust surface (Yurimoto and Kuramoto, 2004). Subsequently, the ^{16}O -poor water ice-bearing dust was then radially drifted to the hot region of the protoplanetary disk to deliver ^{16}O -poor H_2O gaseous reservoirs. Evidence for the presence of ^{16}O -poor H_2O reservoirs in the ancient solar system would be preserved as ^{16}O -poor isotopic compositions of cosmic symplectite (intergrown iron sulfide and oxide assemblage) and cometary water ice (Sakamoto et al., 2007; Seto et al., 2008; Schroeder et al.,

* Corresponding author.

E-mail address: yamamoto.daiki.182@m.kyushu-u.ac.jp (D. Yamamoto).

<https://doi.org/10.1016/j.gca.2024.04.014>

Received 9 November 2023; Accepted 8 April 2024

Available online 18 April 2024

0016-7037/© 2024 The Author(s). Published by Elsevier Ltd. This is an open access article under the CC BY-NC-ND license (<http://creativecommons.org/licenses/by-nc-nd/4.0/>).

2019). Although oxygen isotopic compositions of the CO disk gas based on the direct observations of protoplanetary disks have been poorly constrained (Smith et al., 2009; Furuya et al., 2022), CO gas would be enriched in ^{16}O as water vapor becomes depleted in ^{16}O . The Sun's oxygen isotopic composition, evaluated from the measurements of solar wind particles returned by the *Genesis* spacecraft (McKeegan et al., 2011), is close to those of refractory inclusions and amoeboid olivine aggregates (AOAs) (Yurimoto et al., 2008 and references therein). As the solar isotopic composition is representative of the solar system, this self-shielding model would predict isotopically distinct oxygen isotopic end members (i.e., ^{16}O -poor H_2O gas and ^{16}O -rich CO gas), and oxygen isotope exchange between these end members in the protosolar disk would result in the oxygen isotopic compositions of extraterrestrial materials including the Earth and planets that are distinct from the Sun.

A dominant solid component in the early stage of protosolar disk evolution is thought to be amorphous silicate (e.g., Nuth et al., 2005). We experimentally investigated oxygen isotope exchange kinetics between amorphous silicates and H_2O gas and found that effective oxygen isotope exchange between amorphous silicate with forsterite (Mg_2SiO_4) and enstatite (MgSiO_3) compositions and water vapor occurred under the disk-like low water vapor pressure conditions (Yamamoto et al., 2018, 2020). These amorphous silicates were found to experience oxygen isotope exchange with disk water vapor at temperatures higher than ~ 500 – 650 K within the lifetime of the protosolar disk gas (1–10 Myr; Pascucci and Tachibana, 2010). As gaseous oxygen isotope exchange between CO and H_2O , whose kinetics has been discussed by Alexander (2004) and Lyons et al. (2009), is sluggish at temperatures suitable for the presence of amorphous silicate, the timescale of the oxygen isotope exchange reaction between amorphous silicate and water vapor is always considerably shorter than that of the gas phase isotope equilibrium at a wide range of disk temperatures ($< \sim 1000$ K) (Yamamoto et al., 2020). In this case, amorphous silicates would likely only exchange oxygen isotopes with water vapor, and oxygen isotopic compositions of the silicate dust should reflect the surrounding water vapor in the disk. However, if the amorphous silicate-CO gas isotope exchange reaction is faster than CO- H_2O equilibrium, oxygen isotopic compositions of the CO gas is directly transferred to the silicate grain rather than the indirect slow transfer through the CO- H_2O isotope exchange reaction, and three oxygen isotopic reservoirs would likely reach isotope equilibrium within the shorter timescale. In this case, oxygen isotopic compositions of silicate dust may correspond to the bulk oxygen isotopic compositions of the protosolar disk gas. Therefore, experimental investigations of oxygen isotope exchange between silicate dust and CO gas are vital for understanding of the oxygen isotopic evolution of the disk and solar system. In this study, we report kinetic data on the oxygen isotope exchange reaction between amorphous silicate dust and disk-like low-pressure CO gas.

2. Experiments

2.1. Oxygen isotope exchange experiments

The starting material required for the oxygen isotope exchange experiments in this study is the powdery sample of amorphous silicate with forsterite (Mg_2SiO_4) stoichiometry (hereafter referred to as amorphous forsterite), which was synthesized by an induced thermal plasma method (Koike et al., 2010; Imai, 2012). The starting material is identical to that used in the oxygen isotope exchange experiments between amorphous forsterite and low-pressure water vapor (Yamamoto et al., 2018). Detailed descriptions of the starting material can be found elsewhere (Koike et al., 2010; Imai, 2012; Yamamoto and Tachibana, 2018; Signorile et al., 2020). Oxygen isotope exchange experiments between amorphous forsterite and CO gas were conducted at 673–883 K under the protosolar disk-like low pressure of CO gas (P_{CO}) of 0.05, 0.3, and 1 Pa for 3–330 h. A gold-mirror vacuum furnace (Thermo-Riko GFA 430 VN) equipped with a gas flow system for CO gas, comprising a silica glass

tube (36 mm in diameter and 450 mm in length) surrounded by an Inconel alloy heater and a gold-coated mirror tube, butterfly valve, and a pumping system (a turbomolecular pump and a scroll pump; Hicube 80 Eco, Pfeiffer Vacuum), was used for the experiments. The furnace was the same as that used in our previous experiments (Yamamoto et al., 2018, 2020), but the gas flow system was changed for this study. ^{18}O -enriched CO gas was supplied from a gas cylinder synthesized by Taiyo Nippon Sanso Corp., and its flow rate was controlled by a mass flow controller (Kofloc 3600) (Yamamoto et al., 2022). The gas in the cylinder comprised $\sim 97.2\%$ CO, $\sim 2.2\%$ H_2 , $\sim 0.6\%$ N_2 , and ~ 22 ppm of CO_2 in volume (Yamamoto et al., 2022).

The furnace temperature was monitored and controlled using a type K thermocouple located outside of the silica glass tube (Yamamoto and Tachibana, 2018; Yamamoto et al., 2018, 2020). As the location of the thermocouple is not the same as that of the samples, the temperature calibration of the samples under each P_{CO} condition was made with an uncertainty of ± 5 °C against the melting points of sodium chloride (800.4 °C), potassium bromide (730 °C), lithium bromide (547 °C), and indium (156.6 °C) placed at the sample location (Yamamoto and Tachibana, 2018; Yamamoto et al., 2018, 2020).

Approximately 30 mg of the starting material put in a platinum vessel ($10 \times 15 \text{ mm}^2$ in width and 5 mm in depth) was placed on the silica glass sample stand in the furnace. After the pressure of the entire system, including the CO gas flow line, was reduced to $\sim 1\text{--}4 \times 10^{-4}$ Pa of the total pressure by the pumping system, the gas flow line was filled with 1.1×10^5 Pa of pure CO gas provided from the CO gas cylinder to ensure that the pressure in the gas flow line was higher than that of the surrounding atmosphere. The sample temperature was then slowly increased from room temperature to the desired temperature in 30 min, and CO gas was introduced into the furnace as soon as the sample temperature reached the experimental temperature. The P_{CO} was adjusted by the balance between the gas flow rate controlled by the mass flow controller and the evacuation rate controlled by the butterfly valve. The gas flow rate was set at 0.25, 0.42, and $1.40 \text{ cm}^3 \text{ min}^{-1}$ at $P_{\text{CO}} = 0.05, 0.3, \text{ and } 1$ Pa, respectively. After the sample was maintained at a fixed temperature for a desired duration, CO gas supply was stopped and then the sample was then cooled down to room temperature in ~ 20 min. The fluctuation in the P_{CO} during the experiments was typically less than 10 %.

Time variant oxygen isotope exchange reaction experiments between amorphous forsterite and low-pressure ^{18}O -enriched water vapor were also conducted at 623, 673, and 743 K at a water vapor pressure ($P_{\text{H}_2\text{O}}$) of 0.1 Pa with the same experimental procedure reported in Yamamoto et al. (2018, 2020) to compare the isotope exchange rate with CO gas at low temperatures. Oxygen-18 enriched water ice (97 % ^{18}O ; Taiyo Nippon Sanso Corp.) kept at -20 °C in a freezer (SC-DF25; Twinbird Corp.) was used as the source of water vapor. The amorphous forsterite used here was the same as that used in Yamamoto et al. (2018) and in this study.

The experimental conditions and results are summarized in Table 1. The time required for the amorphous forsterite we used in this study to reach a crystallization degree of 5 % is $\sim 7.4 \times 10^{12}$ and $\sim 4.4 \times 10^{12}$ h at 623 and 883 K, respectively (Yamamoto and Tachibana, 2018), which are larger than the experimental duration (3–330 h) (Table 1), suggesting that the crystallization of amorphous forsterite did not take place under the experimental conditions.

In order to investigate the effect of gas species in the furnace on the kinetics of oxygen isotope exchange between amorphous silicate and C^{18}O gas, gas species in the furnace during the experiments with the sample were monitored by a quadrupole mass spectrometer (QMS; HORIBASTEC QL-SG01-065-1A). QMS analyses were also made during heating in vacuum without the sample to investigate the background gaseous components.

Table 1Experimental conditions and results of the samples heated under various temperature- P_{CO} -duration conditions.

Temp. (K)	Flow gas	Flow gas pressure (Pa)	Duration (h)	$f^{18}O^a$	α^b	No. of analyses ^c
883	$C^{18}O$	1	19.67	0.057 ± 0.004^d	0.057 ± 0.004	50
			42	0.092 ± 0.007	0.091 ± 0.007	50
			65	0.164 ± 0.009	0.165 ± 0.009	50
			3	0.010 ± 0.0004	0.009 ± 0.0004	85
			4	0.011 ± 0.0005	0.010 ± 0.0005	90
			4	0.010 ± 0.0004	0.008 ± 0.0004	90
	$C^{18}O$	0.3	7	0.014 ± 0.001	0.013 ± 0.001	90
			16	0.037 ± 0.003	0.036 ± 0.003	90
			20	0.044 ± 0.003	0.043 ± 0.003	90
			24	0.051 ± 0.03	0.050 ± 0.003	86
			48	0.095 ± 0.007	0.095 ± 0.007	80
			26	0.018 ± 0.002	0.016 ± 0.002	50
			48	0.043 ± 0.004	0.042 ± 0.004	50
			72	0.060 ± 0.004	0.059 ± 0.004	50
			42	0.074 ± 0.006	0.073 ± 0.006	50
			65	0.106 ± 0.007	0.106 ± 0.007	50
			69	0.111 ± 0.006	0.111 ± 0.006	50
			120	0.197 ± 0.006	0.199 ± 0.007	50
	$C^{18}O$	0.3	3	0.008 ± 0.0003	0.006 ± 0.0004	108
			16	0.035 ± 0.003	0.033 ± 0.004	51
			24	0.027 ± 0.004	0.025 ± 0.004	57
			48	0.077 ± 0.007	0.077 ± 0.007	63
			115	0.168 ± 0.009	0.170 ± 0.009	80
			47	0.023 ± 0.001	0.022 ± 0.002	50
853	$C^{18}O$	0.3	66	0.040 ± 0.003	0.039 ± 0.003	50
			68	0.044 ± 0.003	0.042 ± 0.003	140
			70	0.038 ± 0.003	0.037 ± 0.003	80
			70	0.056 ± 0.004	0.055 ± 0.004	50
			90	0.054 ± 0.003	0.053 ± 0.003	160
			141	0.076 ± 0.005	0.076 ± 0.005	50
	$C^{18}O$	0.05	20	0.032 ± 0.002	0.031 ± 0.002	50
			41.08	0.053 ± 0.002	0.053 ± 0.002	50
			74	0.075 ± 0.005	0.075 ± 0.005	50

Table 1 (continued)

Temp. (K)	Flow gas	Flow gas pressure (Pa)	Duration (h)	$f^{18}O^a$	α^b	No. of analyses ^c
883	$C^{18}O$	0.3	119	0.107 ± 0.004	0.108 ± 0.004	50
			3	0.008 ± 0.0004	0.006 ± 0.0004	50
			18	0.027 ± 0.0009	0.026 ± 0.0009	208
			27	0.034 ± 0.002	0.033 ± 0.002	55
			67	0.075 ± 0.004	0.075 ± 0.004	50
			177	0.145 ± 0.002	0.146 ± 0.002	159
	$C^{18}O$	0.05	65	0.035 ± 0.003	0.033 ± 0.003	80
			90	0.046 ± 0.004	0.045 ± 0.004	80
			168	0.076 ± 0.002	0.075 ± 0.003	80
			312	0.120 ± 0.004	0.120 ± 0.005	80
			67	0.049 ± 0.001	0.048 ± 0.001	50
			120	0.076 ± 0.003	0.076 ± 0.003	50
753	$C^{18}O$	0.3	160	0.101 ± 0.002	0.101 ± 0.002	50
			72	0.033 ± 0.0007	0.031 ± 0.0007	50
			144	0.045 ± 0.0007	0.044 ± 0.0007	50
			240	0.062 ± 0.002	0.062 ± 0.002	50
			330	0.072 ± 0.002	0.071 ± 0.002	50
			673	0.028 ± 0.0007	0.026 ± 0.0007	50
	$C^{18}O$	0.3	90	0.030 ± 0.0008	0.029 ± 0.0008	50
			114	0.036 ± 0.0006	0.035 ± 0.0006	50
			208	0.050 ± 0.001	0.049 ± 0.001	50
			24	0.015 ± 0.0002	0.014 ± 0.0002	100
			91	0.026 ± 0.0003	0.024 ± 0.0003	100
			118	0.029 ± 0.0003	0.027 ± 0.0003	95
743	$C^{18}O$	0.3	140	0.035 ± 0.0004	0.034 ± 0.0004	99
			24	0.096 ± 0.002	0.097 ± 0.002	30
			40	0.106 ± 0.002	0.107 ± 0.002	30
			70	0.129 ± 0.003	0.131 ± 0.003	30
			166	0.167 ± 0.002	0.170 ± 0.002	30
			673	0.048 ± 0.0008	0.047 ± 0.0008	30
	$H_2^{18}O$	0.1				
	$H_2^{18}O$	0.1	45	0.048 ± 0.0008	0.047 ± 0.0008	30

(continued on next page)

Table 1 (continued)

Temp. (K)	Flow gas	Flow gas pressure (Pa)	Duration (h)	$f^{18}\text{O}^a$	α^b	No. of analyses ^c
648	H_2^{18}O	0.1	70	0.057 ± 0.0009	0.057 ± 0.0010	29
			120	0.061 ± 0.001	0.061 ± 0.001	30
			254	0.075 ± 0.002	0.075 ± 0.002	29
			48	0.029 ± 0.0007	0.028 ± 0.0008	30
			66.5	0.035 ± 0.0007	0.034 ± 0.0007	30
			110	0.042 ± 0.0007	0.041 ± 0.0007	30
			284	0.047 ± 0.001	0.046 ± 0.001	30
			63	0.032 ± 0.0008	0.031 ± 0.0008	30
			88	0.042 ± 0.001	0.041 ± 0.002	30
			93	0.037 ± 0.001	0.036 ± 0.001	30
623	H_2^{18}O	0.1	114	0.045 ± 0.001	0.045 ± 0.001	30
			210	0.047 ± 0.001	0.047 ± 0.001	30
			Amorphous forsterite (starting material) ^e	$(2.05 \pm 0.001) \times 10^{-3}$	$\equiv 0$	40

^a Defined as $^{18}\text{O}/(^{18}\text{O} + ^{16}\text{O})$.

^b Defined as $(f^{18}\text{O}_{\text{sample}} - f^{18}\text{O}_{\text{starting material}}) / f^{18}\text{O}_{\text{gas}}$.

^c Number of point analyses by SIMS.

^d All the errors are 2-sigma standard errors.

^e Typical analytical data for the starting material.

2.2. Sample analysis

The particle size distribution of the starting material was measured with a laser diffraction/scattering particle size distribution analyzer (Horiba LA-960V2) at Horiba Instruments Inc. The starting material was dispersed in ethanol using an ultrasonic homogenizer (Nissei Corp. US-600AT, 600 W, 19.5 kHz) for 10 min to eliminate particle agglomeration. Ten min was chosen as the duration of homogenization because the observed size distribution did not change after a dispersion time of more than 5 min. The analysis was conducted thrice under the same sample preparation and analytical methods to ensure reproducibility.

The analytical procedure of oxygen isotopic compositions of amorphous silicate samples is similar to that described in Yamamoto et al. (2020). Oxygen isotope compositions of the starting material and run products were measured by secondary ion mass spectrometry (SIMS) using a Cameca ims-1280HR instrument at Hokkaido University. For SIMS measurements, the sample powder was shaped into a pellet (3 mm diameter) to ensure a flat analytical surface, and the pellet was sintered in a vacuum furnace (Takigawa et al., 2009; Mendybaev et al., 2021; Kamibayashi et al., 2021) at total pressure with the orders of 10^{-5} – 10^{-4} Pa and 1150 °C for 17–24 h. Oxygen isotope exchange between the sample and surrounding atmosphere during sintering was prevented by vacuum heating to maintain the original oxygen isotopic compositions of the samples (Yamamoto et al., 2018, 2020). The amorphous sample in the pellet was transformed into crystalline forsterite by sintering, but this did not affect the oxygen isotope and chemical analyses as the kinetic evaporation of forsterite at 1150 °C in vacuum is negligible (Takigawa et al., 2009). The sintered pellets were mounted into epoxy resin and polished down to a roughness of 1 μm and were then measured

by SIMS using the measurement procedure reported in Kawasaki et al. (2018) and Yamamoto et al. (2020). A focused $^{133}\text{Cs}^+$ primary beam (20 keV, ~1 or ~3 nA) with a diameter of ~15 μm was used for the measurements. The primary beam was first rastered over a $30 \times 30 \mu\text{m}^2$ area for 30 s for intensity stabilization (presputtering). The raster size of the primary beam was then reduced to the $10 \times 10 \mu\text{m}^2$ area, and negative secondary ions ($^{16}\text{O}^-$ and $^{18}\text{O}^-$) were measured simultaneously in the multicollection mode using two Faraday cups with $10^{10} \Omega$ resistors for 40 s. The magnetic field was controlled by a nuclear magnetic resonance (NMR) probe. The mass resolution of $M/\Delta M$ was set at ~2000. A normal incidence electron flood gun was used for the electrostatic charge compensation of the analyzed area during the measurements. Backgrounds of the Faraday cup detectors were collected by signals without the injection of secondary ions during pre-sputtering for each analytical run. Russian spinel ($\delta^{18}\text{O} = 8.5 \%$ relative to standard mean ocean water (SMOW); Yurimoto et al., 1994) was used as a standard to correct the instrumental mass fractionation. Reproducibility (2SD (2-sigma standard deviation) per mean value) of the measured $^{18}\text{O}/(^{16}\text{O} + ^{18}\text{O})$ of the Russian spinel was typically ~0.04 %, whereas that of the sintered starting materials was better than 1.0 %. The oxygen isotopic compositions of the run products were determined as an average of 29–208 spot analyses and their associated errors are assigned as 2-sigma standard error (2SE) of the multiple analyses. The number of the point analyses of each of the run product depends on the homogeneity of the oxygen isotopic compositions in the pellet.

3. Results

3.1. Grain size distribution

The size distribution of the starting material was estimated assuming a perfect spherical shape. This spherical assumption is valid for the ITP-synthesis starting material (Koike et al., 2010; Imai, 2012; Yamamoto et al., 2018; Signorile et al., 2020). The grain size distribution averaged over three repeated analyses, evaluated by the volume of particles, is shown in Fig. 1. The volume-weighted size distribution has a single peak ranging from ~20 nm and 200 nm in radius. The observed size distribution of the sample is asymmetrical and can be explained by the log-normal size distribution expressed as follows;

$$f(r) = \frac{A}{\sqrt{2\pi}r} \exp \left[-\frac{1}{2} \left(\frac{\ln(r/\bar{r})}{\ln\sigma} \right)^2 \right] \quad (1)$$

where A is the scaling factor, r is the median radius, and σ is the geometric standard deviation. The distribution was well fitted with Eq. (1) with an r of 72 nm and σ of 1.43. The mode grain diameters were

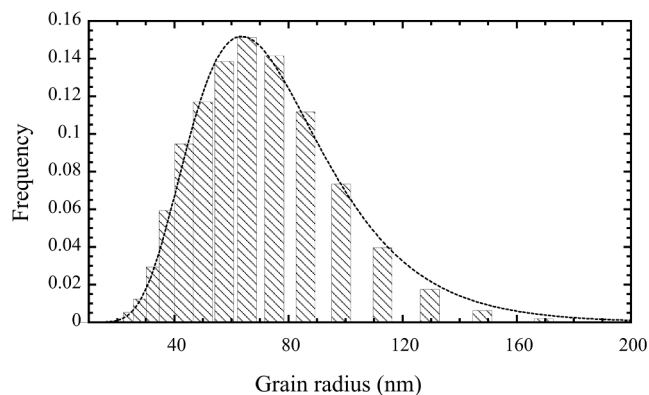


Fig. 1. The volume-weighted particle size distribution of the starting material measured by a laser diffraction/scattering particle size distribution analyzer. The dotted curve represents the best-fitted log-normal distribution function (Eq. (1)). r and σ of 72 nm and 1.43 were obtained, respectively.

estimated to be 127 nm and 82 nm when evaluated by particle volume and number, respectively. Both the size distribution and mode grain diameter are similar to those reported for the same amorphous forsterite (~20–200 nm in size range, 80 nm in average diameter) (Koike et al., 2010; Imai, 2012; Yamamoto et al., 2018; Signorile et al., 2020). Notably, the observed size distribution would not be altered during oxygen isotope exchange experiments owing to the low-temperature annealing in the present experiments (Koike et al., 2010; Yamamoto et al., 2020); thus, this size distribution is applicable to all samples in the present experiments. The calculated volume-weighted size distribution of the starting material with a bin width of 2.5 nm in the grain diameter range of 20–200 nm was used for the calculation, as described below.

3.2. Gas species monitored by QMS

QMS spectra during the isotope exchange experiments with CO gas show that C^{18}O gas is the most dominant gas species. (Fig. 2). Cracking of the C^{18}O gas owing to electron impact ionization leads to the formation of $^{18}\text{O}^+$ ($m/z = 18$) with an O^+/CO^+ value of ~0.01 (Ram-anjaneyulu et al., 2014; Yamamoto et al., 2022), which is consistent with the indicated partial pressure at m/z of 18. Yamamoto et al. (2022) found that ^{18}O -rich water vapor ($m/z = 20$) was formed during isotope exchange experiments at ~1400 °C between calcium-aluminum-rich inclusion (CAI) melt and C^{18}O gas through oxygen isotope exchange between the C^{18}O gas and isotopically-normal residual water vapor in the furnace and/or chemical reaction between C^{18}O gas and H_2 from the CO gas cylinder. In this study, the peak at $m/z = 20$ was not observed, and its pressure was broadly consistent with the background pressure level (Fig. 2). This suggests that the formation of H_2^{18}O vapor is not likely to proceed effectively under low-temperature heating conditions not in the case of oxygen isotope exchange experiments between CAI melt and C^{18}O gas conducted at much higher temperatures (Alexander, 2004; Lyons et al., 2009; Yamamoto et al., 2022). Isotopically-normal water molecules ($m/z = 18$) residing in the furnace would change the temporal evolution of the isotope exchange rate as discussed below. However, the partial pressure of $\text{H}_2^{16}\text{O}^+$ ($m/z = 18$) could not be determined independently during the experiments with C^{18}O gas (Yamamoto et al., 2022) because it overlaps with the cracking ion ($^{18}\text{O}^+$) of C^{18}O gas. QMS spectra during heating in vacuum (blank experiments) suggest that the most dominant gas was H_2^{16}O with a partial pressure of $\sim 1 \times 10^{-4}$ Pa. This pressure is almost comparable to the total pressure of residual gas during the blank experiments. Therefore, the partial pressure of isotopically-normal water molecules was typically $\sim 1 \times 10^{-4}$ Pa during the isotope exchange experiments with C^{18}O gas.

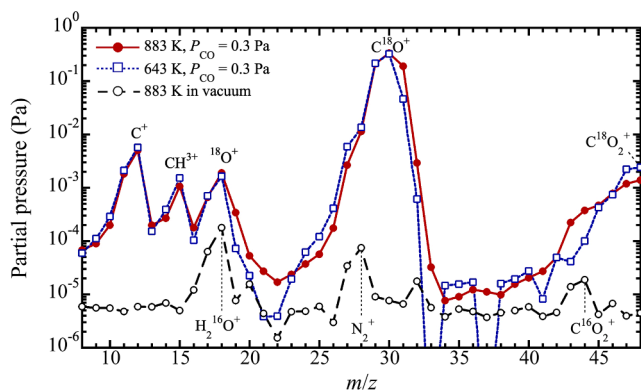


Fig. 2. Typical QMS spectra during experiments with 0.3 Pa of C^{18}O gas at 883 K (red solid curve with closed circles) and 643 K (blue dotted curve with open squares) 2 h after reaching the desired temperatures. A QMS spectrum for the blank experiment in vacuum at 883 K (black dashed curve with open circles) is also shown for comparison.

3.3. Oxygen isotopic compositions of the heated samples with CO gas

Enrichment of ^{18}O in the oxygen isotopic compositions ($^{18}\text{O}/(^{16}\text{O} + ^{18}\text{O}) = f^{18}\text{O}$) of the heated samples relative to those of the starting material ($f^{18}\text{O}_i \sim 0.00204$) are normalized to the isotopic composition of CO gas ($f^{18}\text{O}_{\text{CO}} = 0.98$) to express the degree of isotopic exchange (α) (i. e., $\alpha = (f^{18}\text{O}_{\text{sample}} - f^{18}\text{O}_i) / f^{18}\text{O}_{\text{CO}} = \Delta f^{18}\text{O} / f^{18}\text{O}_{\text{CO}}$) (Yamamoto et al., 2018; 2020). The measured isotopic composition of the starting material on each analytical date was used to obtain the $f^{18}\text{O}_i$ value.

Oxygen isotopic compositions and the values of α for the starting material and heated samples with C^{18}O gas at each heating condition are summarized in Table 1. Oxygen isotope compositions of the heated samples were enriched in ^{18}O relative to those of the starting materials ($f^{18}\text{O}_i \sim 0.00204$), and this enrichment became more prominent with increasing heating duration. Although water vapor is an effective oxygen exchange partner for amorphous silicates (Yamamoto et al., 2018, 2020), it does not become enriched in ^{18}O during the experiments, as discussed above. Therefore, the enrichment in ^{18}O for the heated samples suggests that isotope exchange between amorphous forsterite and C^{18}O gas occurred in the present experiments. It should be noted that variations in the measured $f^{18}\text{O}$ of the heated samples are typically in the range of ~5–40 % (2SD), which is much larger than those of the starting material (<1.0 %). The large variations in oxygen isotopic compositions of the heated samples would be attributed to the presence of the size distribution of the starting material (Fig. 1), and the sintering process for SIMS analysis does not homogenize this isotopic distribution depending on the grain size (Yamamoto et al., 2020). However, this heterogeneity is considerably smaller than the degree of evolution of oxygen isotopic compositions of the heated samples, and it does not affect the discussion below. Evaluation of the temporal changes of α with kinetic models with a size distribution should be applied to obtain more plausible values of kinetic parameters, which is discussed in detail below.

3.4. Oxygen isotopic compositions of the heated samples with H_2O gas

Oxygen isotopic compositions of the heated samples with H_2^{18}O gas at 623, 673, and 743 K under $P_{\text{H}_2\text{O}}$ of 0.1 Pa were also enriched in ^{18}O compared with the starting materials, suggesting the oxygen isotope exchange between amorphous forsterite and H_2O gas occurred (Table. 1).

4. Discussion

4.1. Oxygen isotope exchange kinetics at 883–753 K and P_{CO} of 0.05, 0.3, and 1 Pa

Fig. 3 shows the temporal changes of α at 883, 853, 803, and 753 K under P_{CO} of 0.3 Pa. The α values obtained in the study are compared with those calculated based on the experimental data between amorphous forsterite and 0.3 Pa of water vapor at each temperature (Yamamoto et al., 2018). Notably, the rate of oxygen isotope exchange of amorphous forsterite with CO gas is several- to 100-fold smaller than that with H_2O gas under the same temperature and partial pressure conditions.

Temperature and P_{CO} dependencies of the temporal change of α at 883–753 K and P_{CO} of 0.05–1 Pa are shown in Figs. 4 and 5, respectively. The temporal changes of α depend on both temperature and P_{CO} , wherein α increases with increasing temperature and P_{CO} . The α values under all T - P_{CO} conditions evolve almost linearly with the heating duration. The linear evolution of α with the heating duration suggests that a gaseous supply to the grain surface is a rate-limiting step (Yamamoto et al., 2018, 2020, 2021, 2022). The rate of the reaction controlled by the supply of the gaseous phase to the grain surface should obey the following equation:

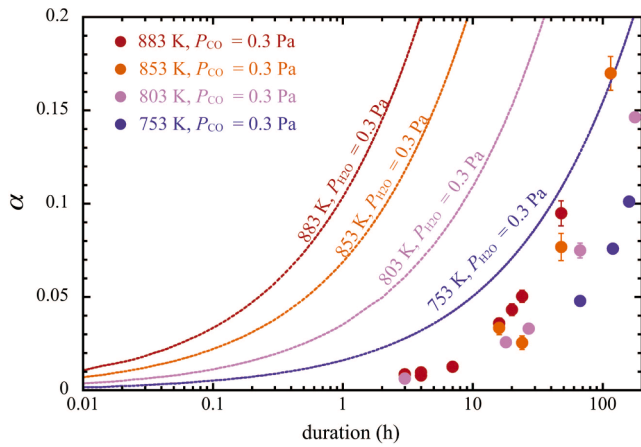


Fig. 3. Temporal changes of oxygen isotopic compositions of the amorphous forsterite samples heated with 0.3 Pa of $C^{18}O$ gas at 883 K (red circles), 853 K (orange circles), 803 K (pink circles), and 753 K (purple circles) compared with the model profiles for O isotope exchange with $H_2^{18}O$ gas at 883 K (red curve), 853 K (orange curve), 803 K (pink curve), and 753 K (purple curve). The error bars represent 2-sigma standard errors. The model curves were calculated as the diffusion-controlled isotope exchange reaction in a sphere (Eq. (6)) using the kinetic data between amorphous forsterite and 0.3 Pa of $H_2^{18}O$ gas from Yamamoto et al. (2018).

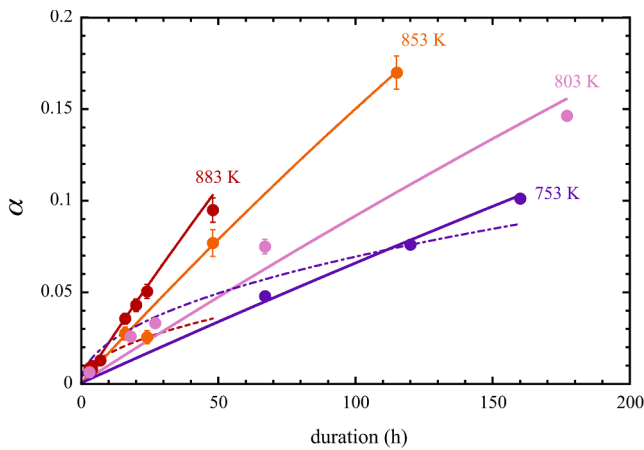


Fig. 4. Temporal changes of the degree of oxygen isotope exchange (α) at 0.3 Pa of $C^{18}O$ gas and 883 K (red circles), 853 K (orange circles), 803 K (pink circles), and 753 K (purple circles). The red, orange, pink, and purple solid curves represent the best-fitted curves of the CO gas supply-controlled reaction for the particles with size distribution (Eq. (5)) at 883, 853, 803, and 753 K, respectively. The best-fitted curves of the three-dimensional diffusion equation for the particles with size distribution (Eq. (7)) at 883 and 753 K are indicated as red dotted and purple dotted-dashed curves, respectively. The error bars represent 2-sigma standard errors.

$$\frac{d\alpha}{dt} = \frac{\beta_{CO} J_{CO} S(1-\alpha)}{\gamma(V/\Omega)N_A} \quad (2)$$

where β_{CO} is a dimensionless parameter that expresses the isotope exchange efficiency of colliding CO gas molecules at the grain surface (Yamamoto et al., 2018, 2020, 2021, 2022), t is the time, J_{CO} is the flux of CO molecules from the vapor, S is the grain surface area, γ is the atom ratio of oxygen in the gas and solid phases (4 for amorphous forsterite and CO molecules), V is the grain volume, Ω is the molar volume of amorphous forsterite, and N_A is Avogadro's number. The gaseous kinetic theory gives J_{CO} as:

$$J_{CO} = \frac{P_{CO}}{\sqrt{2\pi m_{CO} k_B T}} \quad (3)$$

where P_{CO} and m_{CO} are the partial pressure and molecular weight of CO gas, respectively, k_B is the Boltzmann constant, and T is the absolute temperature.

The integral form of Eq. (2) is given by Yamamoto et al., (2018,2020);

$$\alpha = 1 - \exp \left[-\frac{\beta_{CO} J_{CO} S t}{\gamma(V/\Omega)N_A} \right] \quad (4)$$

The particle size distribution in the sample would change the temporal evolution of α , depending on the width of the size distribution (Ritger and Peppas, 1987). For amorphous forsterite with the size distribution (i.e., polydisperse system), Eq. (4) can be modified by considering the individual contribution of a particle having a radius r_i with volume fraction $f(r_i)$ (Ritger and Peppas, 1987), as follows:

$$\alpha = 1 - \sum_i f(r_i) \exp \left[-\frac{\beta_{CO} J_{CO} S(r_i) t}{\gamma(V(r_i)/\Omega)N_A} \right] \quad (5)$$

Another plausible rate-limiting step for oxygen isotope exchange between amorphous silicate and CO gas is the diffusive process of oxygen-bearing species in the amorphous structure (Yamamoto et al., 2018, 2020). The diffusion-controlled oxygen isotope exchange reaction in a sphere (Crank, 1975; Yamamoto et al., 2018, 2020) is expressed as:

$$\alpha = 1 - \sum_{n=1}^{\infty} \frac{6}{n^2 \pi^2} \exp \left(-\frac{D n^2 \pi^2 t}{r^2} \right) \quad (6)$$

where D is the diffusive isotope exchange rate constant, r is the grain radius. Eq. (6) can also be modified for the polydisperse system by considering the size distribution (e.g., Ritger and Peppas, 1987):

$$\alpha = 1 - \sum_i f(r_i) \sum_{n=1}^{\infty} \frac{6}{n^2 \pi^2} \exp \left(-\frac{D n^2 \pi^2 t}{r_i^2} \right) \quad (7)$$

All best-fitted parameters of both reaction equations for the mono-disperse and polydisperse systems are summarized in Table 2. The temporal changes of α at 883, 853, and 803 K and P_{CO} of 0.05, 0.3, and 1 Pa and at 753 K and P_{CO} of 0.3 Pa can be explained by the supply-controlled reaction equations (Eqs. (4) and (5)) rather than the diffusive isotope exchange reaction equations (Eqs. (6) and (7)) (Fig. 5). This indicates that under these conditions, the reaction is controlled by the supply of CO molecules from the vapor phase. We note that the best-fitted curves with both reaction equations for the polydisperse system (Eq. (5)) are similar to those for the monodisperse system (Eq. (4)). The size distribution slightly affects the β_{CO} (Table 2), but barely affects the temporal changes of α , which is likely attributed to the small width of size distribution in the starting material (Fig. 1).

Isotopically-normal residual water molecules may have a reverse effect against $C^{18}O$ gas on the temporal change of α in the present experiments. However, this effect is negligible, as presented in Appendix 1.

The β_{CO} value was found to be $\sim 3 \times 10^{-8}$ – 4×10^{-7} at 753–883 K and P_{CO} of 0.05–1 Pa, which is 2–3 orders of magnitude smaller than that for the re-estimated β_{H_2O} value based on the volume-weighted size distribution of the starting material (1.6×10^{-5} at 883–853 K; Yamamoto et al., 2018) (Fig. 6). This difference in β values for CO and H_2O is consistent with that for the case of CAI melt (~ 0.28 and 10^{-3} – 10^{-4} for β_{H_2O} and β_{CO} , respectively) (Yamamoto et al., 2021, 2022). This consistency suggests that amorphous silicate and silicate melts with different chemical compositions (e.g., amorphous silicate with enstatite ($MgSiO_3$) composition and chondrule melt) likely have similar orders of differences in reactivity with H_2O and CO gases with respect to the surface oxygen isotope exchange reaction.

The β_{CO} value is dependent on P_{CO} ; the β_{CO} increases with decreasing P_{CO} (Fig. 6). This dependence would not be attributed to amorphous

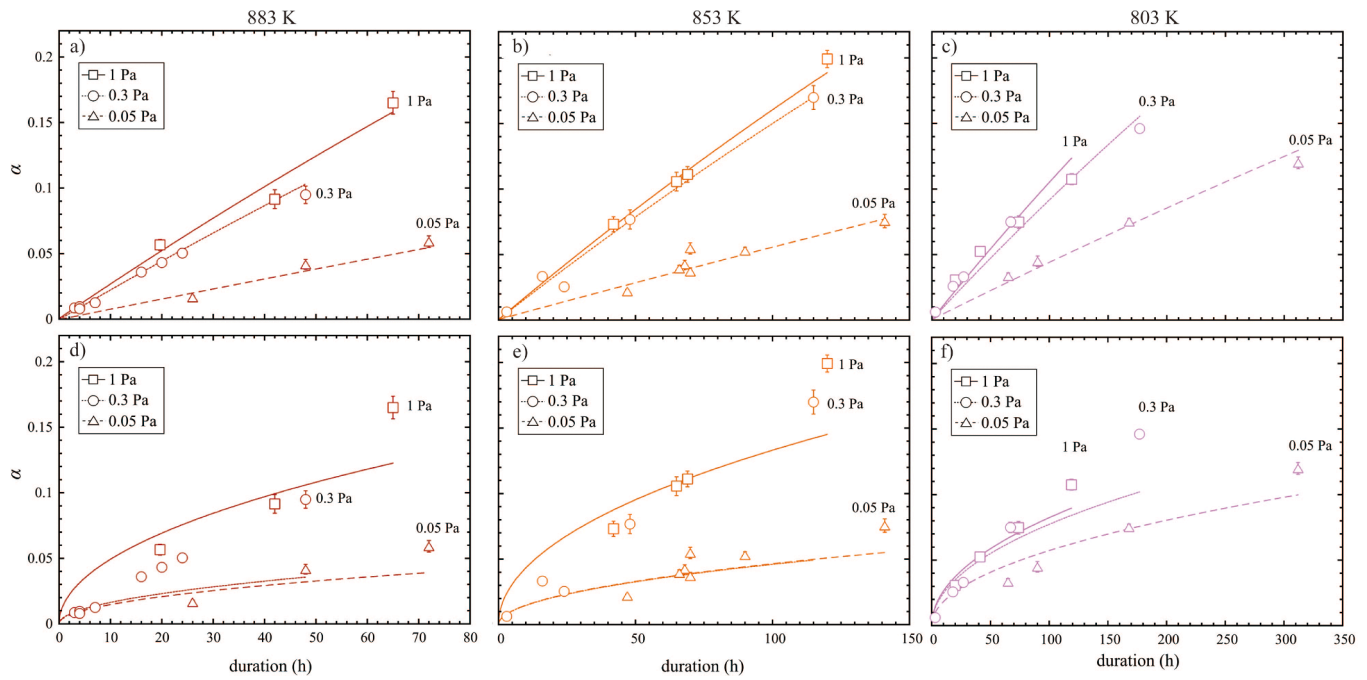


Fig. 5. Temporal changes of the degree of oxygen isotope exchange (α) at 883, 853 K, and 803 K and 1, 0.3, and 0.05 Pa of CO gas. Squares, circles, and triangles represent data at P_{CO} of 1, 0.3, and 0.05 Pa, respectively. The same experimental data are shown in (a) and (d) for 883 K, (b) and (e) for 853 K, and (c) and (f) for 803 K, respectively. Upper figures (a–c) show the fitting results of the experimental data with the CO gas supply-controlled reaction equation for the particles with size distribution (Eq. (5)) under each T - P_{CO} condition. The best-fitting results with the three-dimensional diffusion equation for the particles with size distribution (Eq. (7)) are shown in the lower figures (d–f). The fitting profiles for data at P_{CO} of 1, 0.3, and 0.05 Pa are shown as solid, dotted, and dashed curves, respectively. Error bars are 2-sigma standard errors.

Table 2

Kinetic parameters of β_{CO} and D determined by fitting with the supply- and diffusion-controlled isotope exchange equations (Eqs. (3)–(6)) for monodisperse and polydisperse systems.

Temp. (K)	Flow gas	Flow gas pressure (Pa)	Supply-controlled reaction		Diffusion-controlled reaction	
			Monodisperse ^a	Polydisperse ^b	Monodisperse	Polydisperse
			β_{CO}		D ($\text{m}^2 \text{s}^{-1}$)	
883	C^{18}O	1	$(5.33 \pm 0.76) \times 10^{-8}$ ^c	$(5.72 \pm 0.82) \times 10^{-8}$	/	/
	C^{18}O	0.3	$(1.49 \pm 0.15) \times 10^{-7}$	$(1.63 \pm 0.17) \times 10^{-7}$	/	/
	C^{18}O	0.05	$(3.12 \pm 0.62) \times 10^{-7}$	$(3.37 \pm 0.66) \times 10^{-7}$	/	/
853	C^{18}O	1	$(3.46 \pm 0.14) \times 10^{-8}$	$(3.71 \pm 0.16) \times 10^{-8}$	/	/
	C^{18}O	0.3	$(1.10 \pm 0.21) \times 10^{-7}$	$(1.15 \pm 0.19) \times 10^{-7}$	/	/
	C^{18}O	0.05	$(2.27 \pm 0.25) \times 10^{-7}$	$(2.40 \pm 0.28) \times 10^{-7}$	/	/
803	C^{18}O	1	$(2.13 \pm 0.47) \times 10^{-8}$	$(2.28 \pm 0.48) \times 10^{-8}$	/	/
	C^{18}O	0.3	$(6.11 \pm 1.20) \times 10^{-8}$	$(6.55 \pm 1.18) \times 10^{-8}$	/	/
	C^{18}O	0.05	$(1.71 \pm 0.16) \times 10^{-7}$	$(1.83 \pm 0.16) \times 10^{-7}$	/	/
753	C^{18}O	0.3	$(4.20 \pm 0.26) \times 10^{-8}$	$(4.48 \pm 0.25) \times 10^{-8}$	/	/
703	C^{18}O	0.3	/	/	$(1.63 \pm 0.13) \times 10^{-24}$	$(1.57 \pm 0.14) \times 10^{-24}$
673	C^{18}O	0.3	/	/	$(1.14 \pm 0.12) \times 10^{-24}$	$(1.19 \pm 0.11) \times 10^{-24}$
643	C^{18}O	0.3	/	/	$(7.00 \pm 0.92) \times 10^{-25}$	$(7.97 \pm 1.05) \times 10^{-25}$
743	H_2^{18}O	0.1	/	/	$(2.31 \pm 0.74) \times 10^{-23}$	$(2.54 \pm 0.82) \times 10^{-23}$
673	H_2^{18}O	0.1	/	/	$(3.81 \pm 1.24) \times 10^{-24}$	$(4.23 \pm 1.35) \times 10^{-24}$
648	H_2^{18}O	0.1	/	/	$(1.21 \pm 0.48) \times 10^{-24}$	$(1.45 \pm 0.52) \times 10^{-24}$
623	H_2^{18}O	0.1	/	/	$(1.28 \pm 0.32) \times 10^{-24}$	$(1.53 \pm 0.34) \times 10^{-24}$

^a Fitting for the particles without size distribution.

^b Fitting for the particles with size distribution.

^c All the errors represent 2-sigma standard errors.

forsterite-CO gas back reaction based on the following reasons: (1) the oxygen isotope exchange between C^{16}O gas formed through the isotope exchange and amorphous forsterite would not occur efficiently because of the ^{16}O -rich isotopic compositions of the heated samples (Table 1); (2) a smaller flow rate (i.e., experiments under lower P_{CO} conditions) results in a long residual time around the sample. The β_{CO} should decrease with decreasing the gas flow rate due to the increasing contribution of the back reaction, which is not the case as observed in this study. Therefore,

other factors, such as the adsorption of CO gas in addition to the isotope exchange frequency of the colliding CO gas, would be included in the β_{CO} values.

The temperature dependence of β_{CO} value at each P_{CO} shows the Arrhenius relation as follows (errors are 2 sigma) (Fig. 6);

$$\beta_{\text{CO}, P_{\text{CO}}=0.05 \text{ Pa}} = (1.2 \pm 0.7) \times 10^{-6} \exp \left[-37.7 \pm 13.1 (\text{kJ mol}^{-1}) R^{-1} (1/T - 1/1200) \right] \quad (8)$$

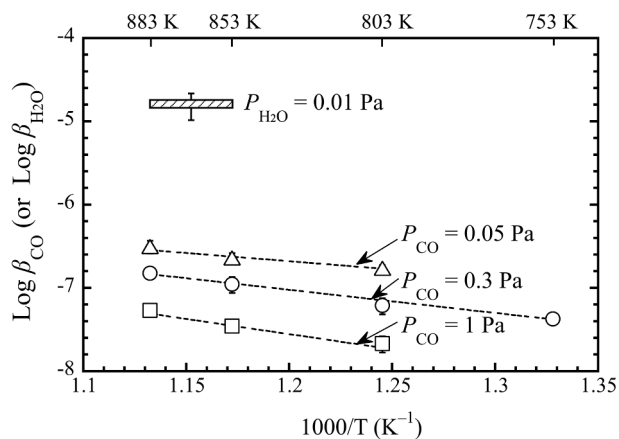


Fig. 6. Arrhenius plot of the non-dimensional parameter β that expresses the isotope exchange efficiency for colliding CO molecules from the gas phase at P_{CO} of 0.05, 0.3, and 1 Pa (triangles, circles, and squares, respectively), and for colliding H_2O molecules (shaded bar) (Yamamoto et al., 2018). The dotted lines represent best-fit draws through the data under each P_{CO} condition (Eqs. (8)–(10)). Error bars are 2-sigma standard errors.

$$\beta_{\text{CO}, P_{\text{CO}}=0.3 \text{ Pa}} = (1.1 \pm 0.3) \times 10^{-6} \exp[-53.9 \pm 4.4 (\text{kJ mol}^{-1})R^{-1}(1/T - 1/1200)] \quad (9)$$

$$\beta_{\text{CO}, P_{\text{CO}}=1 \text{ Pa}} = (6.3 \pm 5.4) \times 10^{-7} \exp[-69.3 \pm 20.8 (\text{kJ mol}^{-1})R^{-1}(1/T - 1/1200)] \quad (10)$$

The term “1/1200” in the above equations was introduced to reduce the uncertainty of the pre-exponential factors as amorphous forsterite readily crystallizes at temperatures higher than ~ 1200 K (Yamamoto and Tachibana, 2018; Yamamoto et al., 2018). The P_{CO} dependencies of the pre-exponential factors ($\beta_{\text{CO}, 0}$) and the activation energies (E_a) were fitted with linear regressions (Fig. 7), and we obtained an Arrhenius relation that considers the P_{CO} dependence of the kinetic parameters as follows (errors are 2 sigma):

$$\beta_{\text{CO}}(T, P_{\text{CO}}) = \{(1.3 \pm 0.2) \times 10^{-6} - (6.2 \pm 3.9) \times 10^{-7} P_{\text{CO}}\} \exp[-\{(43.1 \pm 4.4) + (32.5 \pm 12.9) P_{\text{CO}}\} (\text{kJ mol}^{-1})R^{-1}(1/T - 1/1200)] \quad (11)$$

where P_{CO} is expressed in Pa.

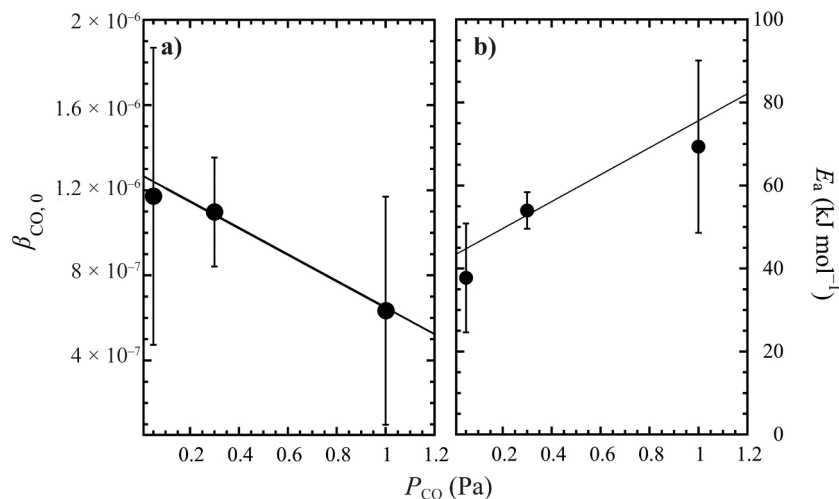


Fig. 7. P_{CO} dependence of the (a) pre-exponential factor of β_{CO} ($\beta_{\text{CO}, 0}$) and (b) the activation energy (E_a) as a function of P_{CO} (Fig. 6). Linear regressions (solid lines) were adopted for both cases. Errors are 2-sigma standard errors.

4.2. Oxygen isotope exchange kinetics at 643–703 K and P_{CO} of 0.3 Pa and at 623–743 K and $P_{\text{H}_2\text{O}}$ of 0.1 Pa

Temporal changes of α at 643, 673, and 703 K under P_{CO} of 0.3 Pa are shown in Fig. 8. In contrast to the experiments at higher temperatures shown in section 4.1 (Figs. 4 and 5), the α does not evolve linearly with the heating duration for the entire heating duration (Fig. 8). These temporal changes of α were better explained by the diffusion-controlled isotope exchange equation in a sphere (Eq. (7)) rather than the supply-controlled isotope exchange equation (Eq. 5) (Fig. 8). Those at 623, 648, 673, and 743 K for the isotope exchange experiments with H_2O gas also follow the diffusion-controlled isotope exchange reaction (Fig. 9). The obtained diffusive isotope exchange rate constants with CO gas ($D_{\text{am, Fo-CO}}$) and with H_2O gas ($D_{\text{am, Fo-H}_2\text{O}}$) in this study, along with the $D_{\text{am, Fo-H}_2\text{O}}$ values reported by Yamamoto et al. (2018), are compared in Fig. 10. The plots from Yamamoto et al. (2018) are recalculated using Eq. (7) as they were originally derived using Eq. (6) by assuming a constant r of 40 nm.

We found a good linear correlation of $D_{\text{am, Fo-CO}}$ values in the

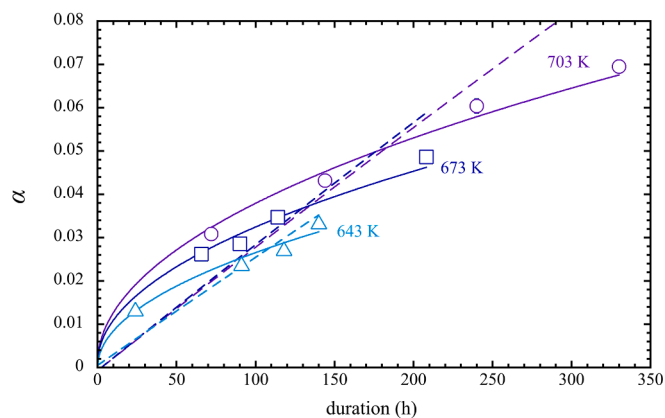


Fig. 8. The temporal changes of the degree of oxygen isotope exchange (α) at 703 (purple), 673 K (dark blue), and 643 K (light blue) for the experiments with P_{CO} of 0.3 Pa. Solid curves represent the best-fitted curves of the three-dimensional diffusion-controlled reaction equation for the particles with size distribution (Eq. (7)) at each temperature. The dotted curves are the best-fitted curves of the CO gas supply-controlled reaction model for the particles with size distribution (Eq. (5)) at each temperature. Two-sigma standard errors of each data point are smaller than the symbol sizes.

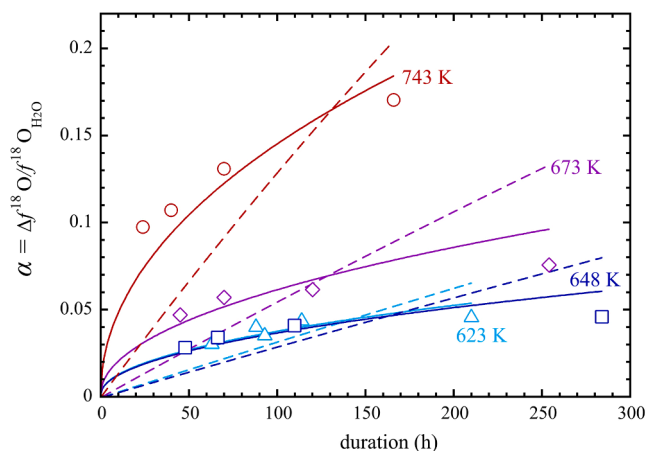


Fig. 9. Temporal changes of the degree of oxygen isotope exchange (α) at 743 K (red circles), 673 K (purple diamonds), 648 K (dark blue squares), and 623 K (light blue triangles) for the experiments with H_2O vapor pressure of 0.1 Pa. Solid curves represent the best-fitted curves of the three-dimensional diffusion-controlled reaction equation for the particles with size distribution (Eq. (7)) at each temperature. The dotted curves are the best-fitted curves of the H_2O gas supply-controlled reaction model for the particles with size distribution (Eq. (5)) at each temperature. Two-sigma standard errors of each data point are smaller than the symbol sizes.

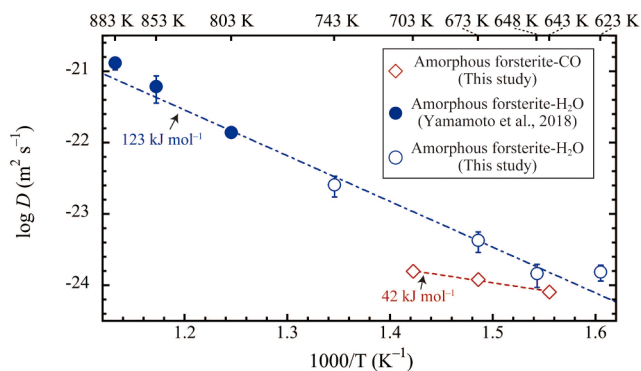


Fig. 10. Comparison of the diffusive isotope exchange rates (D) obtained through the experiments between amorphous forsterite and low-pressure CO gas (red diamonds) and those between amorphous forsterite and low-pressure H_2O gas (blue circles) in the Arrhenius plot. Open and closed blue circles represent the data obtained in this study and in Yamamoto et al. (2018), respectively. All D values are estimated from the diffusion equation in a sphere for a polydisperse system (Eq. (7)). The dotted line represents the best-fit draws for the experiments with CO at 643–703 K. The dotted-dashed line is a best-fit draw through the data at the entire range of the temperatures (623–883 K) for the experiments with H_2O . Error bars represent 2-sigma standard errors.

Arrhenius plot, as follows (errors are 2 sigma):

$$D_{\text{am. Fo-CO}} = (3.1 \pm 2.3) \times 10^{-23} \exp[-41.7 \pm 9.6 (\text{kJ mol}^{-1})R^{-1}(1/T - 1/1200)] \quad (12)$$

$D_{\text{am. Fo-H}_2\text{O}}$ values at 623–743 K obtained in this study combined with those obtained at 803–883 K in Yamamoto et al. (2018) yield the temperature dependence of $D_{\text{am. Fo-H}_2\text{O}}$ as follows (errors are 2 sigma):

$$D_{\text{am. Fo-H}_2\text{O}} = (6.4 \pm 2.1) \times 10^{-20} \exp[-122.7 \pm 5.7 (\text{kJ mol}^{-1})R^{-1}(1/T - 1/1200)] \quad (13)$$

Possible diffusing species for the isotope exchange with CO gas are CO molecules and CO_3^{2-} (Pawley et al., 1992; Morizet et al., 2010; Yoshioka et al., 2019). Oxygen self-diffusion (i.e., diffusion of network oxygen) could be another possible diffusion mechanism as the obtained

diffusive isotope exchange rate constants for the experiments with CO and H_2O gases are similar to each other under the experimental conditions. As diffusive oxygen isotope exchange between silicate glasses and CO gas has not yet been investigated in detail in previous studies, further experimental investigations using silicate glasses with different chemical compositions under various heating conditions are required to reveal the detailed mechanism of the diffusive oxygen isotope exchange between amorphous silicate and CO gas.

4.3. Implication for oxygen isotope evolution in the protosolar disk

Oxygen isotopic evolution in the protosolar disk can be discussed based on the oxygen isotope exchange kinetics between amorphous forsterite and CO (this study), amorphous forsterite and H_2O (this study and Yamamoto et al., 2018), and CO and H_2O (Alexander, 2004). Calculations of the timescales for oxygen isotope exchange of amorphous forsterite with the grain diameters of 0.1 and 1 μm were done because the matrix silicate grains in chondrites have typical grain diameters of up to $\sim 1 \mu\text{m}$ (Pontoppidan and Brearley, 2010 and references therein). Glass with embedded metal and sulfides (GEMS) have typical grain sizes ranging from 0.1–1 μm (Bradley, 1994; Keller and Messenger, 2011). The time required for equilibrium (α of 0.99) of the diffusion-controlled oxygen isotope exchange reaction for the spherical dust is given by $(0.42 r^2 / D)$ (Crank, 1975) using Eqs. (6), (12), and (13). Timescales for α of 0.99 of the isotope exchange reaction governed by the supply of CO and H_2O gases on the grain surface were calculated by Eqs. (4) and (11). The pressures of both CO and H_2O gases would range from 10^{-1} to 10^{-4} Pa in the protosolar disk gas with the solar system composition ($P_{\text{CO}}/P_{\text{H}_2} = P_{\text{H}_2\text{O}}/P_{\text{H}_2} \sim 10^{-3}$), assuming the total pressure ($P_{\text{tot.}}$) ranges from 10^2 to 10^{-1} Pa (Wood and Morfill, 1988; Lodders, 2003). The $\beta_{\text{H}_2\text{O}}$ is defined as a constant value of 1.6×10^{-5} using Eq. (7) from that of Yamamoto et al. (2018). The timescale for gaseous oxygen isotope exchange reaction between CO and H_2O determined by water vapor pressure (Alexander, 2004; Lyons et al., 2009) and that for the crystallization reaction of amorphous forsterite, whose rate is controlled by temperature and water vapor pressure, (Yamamoto and Tachibana, 2018), were also calculated.

Timescale comparisons of the reaction in the system of amorphous silicate-CO- H_2O under the total pressures of 10^2 and 10^{-1} Pa for 0.1 μm -sized amorphous forsterite grains are shown in Fig. 11a and b. The CO- H_2O isotope equilibrium through gaseous oxygen isotope exchange reaction would require temperatures higher than ~ 800 – 850 K within the typical accretion timescale of meteorite parent bodies after CAI formation (~ 1 Myr; Kleine and Rudge, 2011 and references therein).

The timescale of the oxygen isotope exchange reaction between amorphous forsterite and H_2O gas would be controlled by the flux of H_2O gas at the grain surface at temperatures higher than ~ 700 and 1000 K at $P_{\text{tot.}}$ of 10^{-1} and 10^2 Pa, whereas it would be controlled by the diffusional isotope exchange under the lower temperatures, respectively. The temperatures required for the completion of isotope exchange between amorphous forsterite and H_2O is greater than ~ 450 K within 1 Myr.

The timescale of oxygen isotope exchange dramatically increases as a consequence of the crystallization of amorphous forsterite because the oxygen isotope exchange rate between crystalline forsterite and water is considerably smaller than that between amorphous forsterite and water vapor (Fig. 11) (Jaulou et al., 1980; Yamamoto and Tachibana, 2018). Therefore, effective oxygen isotope exchange between forsterite dust and water vapor should occur at temperatures where oxygen isotope exchange precedes the crystallization of amorphous forsterite. The temperatures at which the timescales of oxygen isotope exchange between amorphous forsterite and water vapor are comparable to those of amorphous forsterite crystallization are ~ 850 and 950 K at $P_{\text{tot.}}$ of 10^{-1} and 10^2 Pa, respectively. Therefore, oxygen isotope exchange between amorphous forsterite and H_2O gas would take place at temperature ranges of ~ 450 – 850 K and ~ 450 – 950 K at $P_{\text{tot.}}$ of 10^{-1} and 10^2 Pa, respectively.

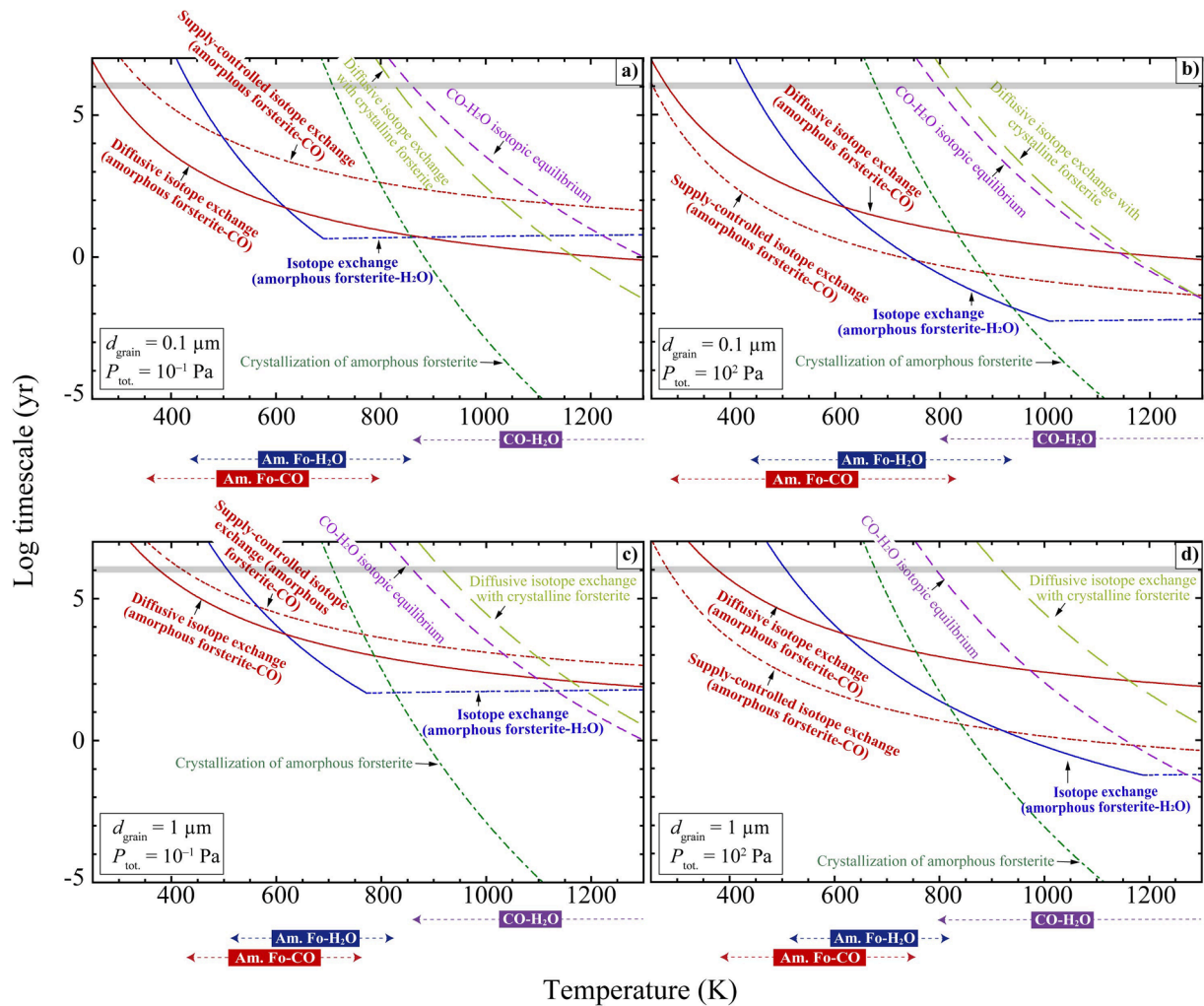


Fig. 11. Timescales of various chemical reactions in amorphous forsterite-CO-H₂O system. Timescales for the oxygen isotope exchange reaction between amorphous forsterite and CO gas with the rate controlled by diffusion in the amorphous structure and the supply of CO are depicted as red solid and red dotted curves, respectively. Blue curves represent the timescales for the isotope exchange between amorphous forsterite and H₂O gas whose rates are controlled by the supply of H₂O gas (dotted) and water diffusion (solid), depending on the temperature and $P_{\text{H}_2\text{O}}$. Green dotted-dashed, purple short-dashed, and light green long-dashed curves represent the timescales of crystallization of amorphous forsterite (Yamamoto and Tachibana, 2018), CO-H₂O gaseous isotope equilibrium (Alexander, 2004; Lyons et al., 2009), and diffusive isotope exchange between crystalline forsterite and disk gas (Jaoul et al., 1980), respectively. Gray-shaded bars indicate the typical meteorite accretion timescale after CAI formation (1 Myr; Kleine et al., 2020 and references therein). Arrows under each figure represent the temperature regions where the isotope equilibria between CO and H₂O, amorphous forsterite and H₂O, and amorphous forsterite and CO are accomplished within the timescale of 1 Myr. Dust diameter and P_{tot} of (a) 0.1 μm and 10^{-1} Pa, (b) 0.1 μm and 10^2 Pa, (c) 1 μm and 10^{-1} Pa, and (d) 1 μm and 10^2 Pa, respectively. Partial pressures of CO and H₂O gas were calculated by considering the solar composition $P_{\text{CO}}/P_{\text{H}_2}$ and $P_{\text{H}_2\text{O}}/P_{\text{H}_2}$ ratios of $\sim 10^{-3}$ (Lodders, 2003). See the text for more details.

The timescales of oxygen isotope exchange reaction between amorphous forsterite and CO gas, controlled by the CO gaseous supply to the grain surface and oxygen isotope diffusion in the amorphous structure, are shown in Fig. 11. These supply- and diffusion-controlled reaction timescales are plotted almost parallel to each other owing to the similar activation energies for these two rate-limiting processes. The oxygen isotope exchange reaction would be controlled by the supply of CO gas to the grain surface at $P_{\text{CO}} = 10^{-1}$ Pa, whereas it would be controlled by the oxygen isotope diffusion in the amorphous structure at $P_{\text{CO}} = 10^2$ Pa. The temperatures where the timescales of oxygen isotope exchange between amorphous forsterite and CO are comparable to those of amorphous forsterite crystallization are ~ 800 and 850 K at P_{tot} of 10^{-1} and 10^2 Pa, respectively. Therefore, oxygen isotope equilibrium between amorphous forsterite and CO gas would be attained at temperature ranges of ~ 350 – 800 K and 300 – 850 K at P_{tot} of 10^{-1} and 10^2 Pa, respectively, within 1 Myr.

Oxygen isotope exchange reactions of amorphous forsterite with both CO and H₂O gases would occur effectively at low temperatures

where gaseous isotope exchange reaction becomes sluggish. This indicates that the oxygen isotopic compositions of CO gas would be transferred directly to the silicate grain rather than the indirect slow transfer through the gaseous isotope exchange reaction at low temperatures. Therefore, amorphous forsterite plays a significant role in accelerating CO-H₂O isotope equilibrium in the protosolar disk. Consequently, the CO-H₂O isotope equilibrium in the disk would be attained much easier (faster) than expected in the previous studies at lower temperatures (Alexander, 2004; Lyons et al., 2009). For instance, at $P_{\text{tot}} = 10^{-1}$ Pa and within 1 Myr, the CO-H₂O isotope equilibrium is achieved by the effective oxygen isotope exchange of amorphous forsterite with both CO and H₂O gases at temperatures of ~ 450 – 800 K, whereas it is achieved through the gaseous isotope exchange reaction only at temperatures higher than ~ 850 K (Fig. 11a). At $P_{\text{tot}} = 10^2$ Pa, the CO-H₂O isotope equilibrium would occur with the aid of amorphous forsterite at temperatures of ~ 450 – 850 K, whereas it would occur through the gaseous isotope exchange reaction only at temperatures higher than ~ 800 K (Fig. 11b). Amorphous forsterite would therefore

play a role in lowering the temperature threshold for the CO-H₂O isotope equilibrium by ~350–400 K in the disk.

For 1 μm -sized amorphous forsterite grains, as in the case of 0.1 μm -sized grains, the oxygen isotope equilibrium in the disk is significantly accelerated by the amorphous forsterite (Fig. 11c and d). The CO-H₂O isotope equilibrium is achieved with the aid of amorphous forsterite at ~500–750 K at $P_{\text{tot.}} = 10^{-1}$ and 10^2 Pa whereas it is only achieved through the gaseous isotope exchange at temperatures higher than ~800–850 K.

Oxygen isotopic evolution of amorphous forsterite dust was also discussed in the evolving dynamic protosolar disk based on the numerical method discussed by Ishizaki et al. (2023), wherein they evaluated effective reaction temperatures (T_{reac}) for various chemical reactions at which a chemical reaction proceeds efficiently before the dust diffuses out from the nearly constant temperature region. This dynamic model is defined as the alpha-viscosity disk model with a mean molecular weight of 2.34 g mol^{-1} , and is based on the assumption that small grains are released at the snow line in the disk (~6–7 au) and are dynamically well coupled with the disk gas, which is adaptable at the grain sizes assumed here. This model considers the motion of dust inward/outward and in the vertical direction through advection and diffusion in the turbulent protoplanetary disk. Detailed descriptions of the dynamic model can be found in Ishizaki et al. (2023).

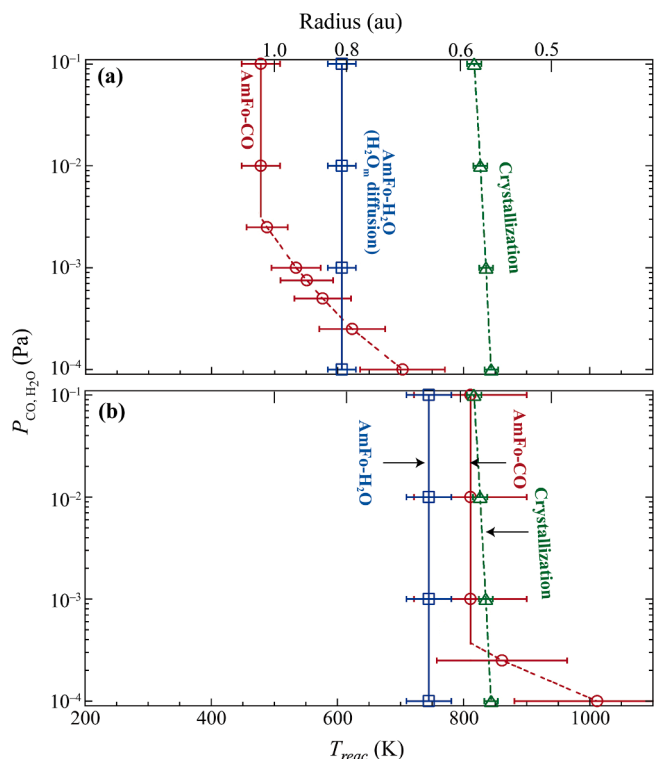


Fig. 12. T_{reac} values for various chemical reactions in amorphous forsterite-CO-H₂O system as a function of P_{CO} or $P_{\text{H}_2\text{O}}$ in a steady accretion solar disk with a mass accretion rate of $10^{-7} M_{\text{Sun}} \text{ yr}^{-1}$ and an alpha viscosity of 10^{-3} . Red open circles are T_{reac} values for the oxygen isotope exchange reaction between amorphous forsterite and CO gas with the rate controlled by diffusion in the amorphous structure (red solid lines) and the supply of CO (red dotted curves). Blue open squares with blue solid lines represent the T_{reac} values for the isotope exchange reaction of amorphous forsterite with the rate controlled by water diffusion. The T_{reac} values for the crystallization of amorphous forsterite are depicted as green open triangles with green dotted-dashed lines. Each error bar represents the dispersions of T_{reac} values (Ishizaki et al., 2023). The upper abscissa represents the corresponding radius from the Sun calculated based on the disk model (Ida et al., 2016) with a mass accretion rate of $10^{-7} M_{\text{Sun}} \text{ yr}^{-1}$ and an alpha viscosity of 10^{-3} . Dust diameters of (a) 0.1 μm and (b) 1 μm . See the text for more details.

Fig. 12 shows the T_{reac} values for the oxygen isotope exchange of amorphous forsterite with CO and H₂O gases and the crystallization of amorphous forsterite in a steady accretion solar disk with a mass accretion rate of $10^{-7} M_{\text{Sun}} \text{ yr}^{-1}$, typical for Sun-like mass stars (Manara et al., 2022), and a dimensionless alpha viscosity of 10^{-3} (Sano et al., 2004). Amorphous forsterite grains with diameters of 0.1 and 1 μm were also assumed. Diffusional isotopic exchange between amorphous forsterite and H₂O was observed at lower temperatures, as shown in Fig. 11. Therefore, the T_{reac} values for the isotope exchange controlled by the water diffusion were only calculated because the protoplanetary dust released at the snow line are generally considered to migrate inward from the outer cold region of disks. We note that, although amorphous forsterite grains experience different pressure environments during their migration in the disk, a single reaction kinetics for each chemical process was adopted for evaluating the T_{reac} values under certain P_{CO} and $P_{\text{H}_2\text{O}}$ conditions because the change in the reaction kinetics associated with the change in surrounding pressure was not considered in the model of Ishizaki et al. (2023). The T_{reac} values of the chemical processes with pressure-dependent reaction rates, such as the supply-controlled isotope exchange between amorphous forsterite and CO gas, would likely be affected, but the above assumption was adopted here for simplicity.

For 0.1 μm -sized amorphous forsterite grains, oxygen isotope exchange of amorphous forsterite with CO gas would be controlled by diffusion at P_{CO} higher than $\sim 3 \times 10^{-3}$ Pa, whereas it is controlled by gaseous supply to the grain surface at lower P_{CO} (Fig. 12a), as shown in Fig. 11. Oxygen isotope exchange of amorphous forsterite with CO and H₂O gases would effectively take place at temperatures of ~475–700 K and ~600 K, respectively, whereas crystallization effectively proceeds at much higher temperatures of ~800–850 K. This suggests that oxygen isotope exchange of 0.1 μm -sized amorphous forsterite grains with both CO and H₂O gases (i.e., oxygen isotope equilibrium in the protosolar disk) would be completed before the onset of its crystallization in the steadily accreting disk. Amorphous forsterite grains kept at temperatures lower than ~475 K would preserve their original isotopic compositions, whereas those experienced at temperatures higher than 600–700 K would obtain the equilibrium oxygen isotopic compositions. The critical temperatures of ~600–700 K for the case of the accelerated isotope exchange reaction by amorphous forsterite is considerably lower than those required for the isotope equilibrium through gaseous isotope exchange (e.g., >~800 K within the timescale of 1 Myr) (Fig. 11). The corresponding reaction timescale for the oxygen isotope equilibrium at temperatures higher than these critical temperatures would be less than $\sim 10^2$ – 10^3 yr (Fig. 11), suggesting that oxygen isotope equilibrium would be reached within the timescales of $< \sim 10^2$ – 10^3 yr and does not require a prolonged period of time such as ~1 Myr. The region at ~600–800 K, where the isotope equilibrium is attained before crystallization of amorphous forsterite proceeds effectively in the steadily accreting disk, would correspond to the radial distance from the Sun of ~0.6–0.8 au based on the disk model by Ida et al. (2016), implying that oxygen isotope equilibrium accelerated by amorphous forsterite is a local process. However, the calculation results that T_{reac} 's for oxygen isotope exchange of amorphous forsterite with CO and H₂O gases do not overlap with that for the crystallization of amorphous forsterite (Fig. 12a). This suggests that, because the dust generally migrates inward in the disk, the temperature region of ~600–800 K would play an effective reaction boundary, and the oxygen isotope equilibrium in the amorphous silicate-CO-H₂O system would be achieved inside of it. Hence, the oxygen isotope exchange reaction processes in this region would significantly affect the evolution of oxygen isotopic compositions of dust and gas at the inner region of the protosolar disk up to ~0.6–0.8 au. In summary, the isotope exchange reaction process of amorphous forsterite with both CO and H₂O gases would take place at ~0.6–0.8 au and be completed within the timescales of $< \sim 10^2$ – 10^3 yr, and this process would affect the oxygen isotopic evolution of dust and gas in the inner region (< 0.6 – 0.8 au) of the protosolar disk.

Oxygen isotope exchange of 1 μm -sized amorphous forsterite with

CO and H₂O gases would take place at higher temperatures of ~750–1000 K compared with that of 0.1 µm-sized grains (~475–700 K) (Fig. 12). The T_{reac} values for the isotope exchange (~750–1000 K) are similar to or overlapped with those for the crystallization of amorphous forsterite (~800–850 K) within the dispersions of the reaction temperatures (Fig. 12b). This suggests that some amorphous forsterite grains would have crystallized before the completion of oxygen isotope exchange with the gas and would possess various isotopic compositions. Consequently, they would likely preserve their oxygen isotopic compositions at the time of crystallization (Yamamoto et al., 2018).

We note that silicate grains with sizes smaller than ~0.1 µm in diameter in primitive meteorite matrices were reported. Buseck and Hua (1993) reported that phyllosilicates in the Orgueil meteorite matrices have small grain sizes of ~5 nm. In addition, highly energetic processes such as cosmic ray irradiation in the interstellar medium, giant collisions, magnetic reconnection events, lightning, and shock waves in the protosolar disk would render silicate a more effective reactant (catalyst) compared with glassy silicate condensates simulated in this study. All of these factors would lead to a smaller isotope equilibrium timescale in the amorphous silicate-CO-H₂O system, and thus the calculated lower limit of critical temperatures for oxygen isotope exchange of amorphous forsterite presented in Figs. 11 and 12 could be regarded as the upper limits for oxygen isotopic equilibration, providing a possibility that oxygen isotope exchange reaction occurs at much lower temperatures and the original isotopic signatures of silicate dust were erased even at definitive low-temperature regions inside the snow line.

If the isotope equilibrium would be attained more easily and effectively through the oxygen isotope exchange of amorphous forsterite grains with both CO and H₂O gases, one would expect that the CO/H₂O ratios and isotopic composition of each gas are the most important parameters to address the oxygen isotopic evolution of silicate dust in the early Solar System. These parameters would have varied temporally and spatially (e.g., Krot et al., 2006; Kawasaki et al., 2018; Krot et al., 2022; Marrocchi et al., 2024), and therefore a detailed theoretical work using the kinetics parameters presented in this study should be done to quantitatively understand the oxygen isotopic compositions of silicate in the Solar System.

5. Conclusions

We experimentally determined the oxygen isotope exchange mechanism and kinetics of the oxygen isotope exchange reaction between amorphous forsterite nanoparticles and low-pressure CO gas of 0.05–1 Pa at 643–883 K. The temporal changes of oxygen isotopic compositions of the samples heated at 753 K and P_{CO} of 0.3 Pa and at 803–883 K and P_{CO} of 0.05–1 Pa can be explained by the CO gas supply-controlled reaction model, wherein the isotope exchange efficiency of colliding CO molecules at the grain surface is 2–3 orders of magnitude smaller than that for water molecules. On the other hand, the temporal changes of the O-isotopic compositions of the samples heated at lower temperatures of 643–703 K and P_{CO} of 0.3 Pa obey the diffusion-controlled reaction model with the rate constant of D (m²/s) = $(3.1 \pm 2.3) \times 10^{-23} \exp[-41.7 \pm 9.6 \text{ (kJ mol}^{-1}\text{)} R^{-1} (1/T-1/1200)]$.

The comparison of timescales of oxygen isotope exchange in the system of amorphous forsterite-CO-H₂O suggests that the isotope exchange reaction rate of amorphous forsterite with both CO and H₂O is much faster than the CO-H₂O gaseous isotope exchange rate at temperatures unsuitable for amorphous forsterite crystallization. This indicates that amorphous forsterite would accelerate gaseous isotopic equilibrium through isotope exchange with both CO and H₂O. We found that for 0.1 µm-sized grains, oxygen isotope exchange of amorphous forsterite with CO and H₂O occurred at lower temperatures before the onset of crystallization, and that the oxygen isotopic equilibrium in a system of amorphous forsterite-CO-H₂O would be attained at temperatures higher than ~600–700 K in the dynamically accreting protosolar disk. The kinetics of the amorphous silicate-CO-H₂O system in this study

should be incorporated into studies on the oxygen isotope evolution of silicate dust and gas in the early solar system.

CRedit authorship contribution statement

Daiki Yamamoto: Writing – review & editing, Writing – original draft, Investigation, Funding acquisition, Formal analysis, Data curation, Conceptualization. **Noriyuki Kawasaki:** Writing – review & editing, Supervision, Data curation. **Shogo Tachibana:** Writing – review & editing, Supervision, Conceptualization. **Lily Ishizaki:** Writing – review & editing, Data curation. **Ryosuke Sakurai:** Writing – review & editing, Data curation. **Hisayoshi Yurimoto:** Writing – review & editing, Supervision, Conceptualization.

Data availability

Data are available through Kyushu University Institutional Repository (QIR) at <https://doi.org/10.48708/7153593>.

Declaration of competing interest

The authors declare that they have no known competing financial interests or personal relationships that could have appeared to influence the work reported in this paper.

Acknowledgments

The authors thank Alexander N. Krot and Joseph A. Nuth for their constructive reviews and comments that improved this paper greatly. Ann Nguyen (AE) is also appreciated for editorial handling. We are grateful to Akira Tsuchiyama and Junya Matsuno for providing the amorphous forsterite powder. This work was financially supported by the Ministry of Education, Sports, Science and Technology KAKENHI grants (19H00712, 21K13986).

Appendix A. Supplementary material

We discussed the effect of residual water molecules in the furnace on β_{CO} in the supplementary file. Supplementary material to this article can be found online at <https://doi.org/10.1016/j.gca.2024.04.014>.

References

- Alexander, C.M.O'D., 2004. Chemical equilibrium and kinetics constraints for chondrule and CAI formation conditions. *Geochim. Cosmochim. Acta* 68, 3943–3969.
- Bradley, J.P., 1994. Chemically anomalous, preaccretionally irradiated grains in interplanetary dust from comets. *Science* 265, 925–929.
- Buseck, P.R., Hua, X., 1993. Matrices of carbonaceous chondrite meteorites. *Annu. Rev. Earth Planet. Sci.* 21, 255–305.
- Clayton, R.N., Grossman, L., Mayeda, T.K., 1973. A component of primitive nuclear composition in carbonaceous chondrites. *Science* 182, 485–488.
- Crank, J., 1975. *The Mathematics of Diffusion*, 2nd ed. Oxford University Press, Oxford, UK, 421 p.
- Furuya, K., Tsukagoshi, T., Qi, C., Nomura, H., Cleaves, L.I., Lee, S., Yoshida, T., 2022. Detections of HCl₁₈O⁺ in a protoplanetary disk: Exploring oxygen isotope fractionation of CO. *Astrophys. J.* 926, 148.
- Ida, S., Guillot, T., Morbidelli, A., 2016. The radial dependence of pebble accretion rates: A source of diversity in planetary systems. *Astron. Astrophys.* 591, A72.
- Imai, Y., 2012. Experimental study of circumstellar silicate dust evolution by crystallization processes using laboratory infrared spectroscopy. Ph.D Thesis. Osaka University, Osaka, Japan.
- Ishizaki, L., Tachibana, S., Okamoto, T., Yamamoto, D., Ida, S., 2023. Effective reaction temperatures of irreversible dust chemical reactions in a protoplanetary disk. *Astrophys. J.* 957, 47 (13 pp).
- Jaoul, O., Froidevaux, C., Durham, W.B., Michaut, M., 1980. Oxygen self-diffusion in forsterite: Implications for the high-temperature creep mechanism. *Earth Planet Sci. Lett.* 47, 391–397.
- Kamibayashi, M., Tachibana, S., Yamamoto, D., Kawasaki, N., Yurimoto, H., 2021. Effect of hydrogen gas pressure on calcium-aluminum-rich inclusion formation in the protoplanetary disk: A Laboratory simulation of open-system melt crystallization. *Astrophys. J. Letters* 923, L12.
- Kawasaki, N., Simon, S.B., Grossman, L., Sakamoto, N., Yurimoto, H., 2018. Crystal growth and disequilibrium distribution of oxygen isotopes in an igneous CA-Al-rich

- inclusion from the Allende carbonaceous chondrite. *Geochim. Cosmochim. Acta*. 221, 318–341.
- Keller, L.P., Messenger, S., 2011. On the origins of GEMS grains. *Geochim. Cosmochim. Acta*. 75, 5336–5365.
- Kleine, T., Rudge, J.F., 2011. Chronology of meteorites and the formation of the Earth and Moon. *Elements* 7, 41–46.
- Koike, C., Imai, Y., Chihara, H., Suto, H., Murata, K., Tsuchiyama, A., Tachibana, S., Ohara, S., 2010. Effects of forsterite grain shape on infrared spectra. *Astrophys. J.* 709, 983–992.
- Krot, A.N., Yurimoto, H., McKeegan, K.D., Leshin, L., Chaussido, M., Libourel, G., Yoshitake, M., Huss, G.R., Guan, Y., Zanda, B., 2006. Oxygen isotopic compositions of chondrules: Implications for evolution of oxygen isotopic reservoirs in the inner solar nebula. *Chem. Der Erde*. 66, 249–276.
- Krot, A.N., Doyle, P.M., Nagashima, K., Dobrica, E., Petaev, M.I., 2022. Mineralogy, petrology, and oxygen-isotope compositions of magnetite \pm fayalite assemblages in CO3, CV3, and LL3 chondrites. *Meteoritic. Planet. Sci.* 57, 392–428.
- Lodders, K., 2003. Solar system abundances and condensation temperatures of the elements. *Astrophys. J.* 591, 1220–1247.
- Lyons, J.R., Young, E.D., 2005. CO self-shielding as the origin of oxygen isotope anomalies in the early solar nebula. *Nature* 435, 317–320.
- Lyons, J.R., Bergin, E.A., Ciesla, F.J., Davis, A.M., Desch, S.J., Hashizume, K., Lee, J.E., 2009. Timescales for the evolution of oxygen isotope compositions in the solar nebula. *Geochim. Cosmochim. Acta*. 73, 4998–5017.
- Manara, C.F., Ansdell, M., Rosotti, G.P., Hughes, A.M., Armitage, P.J., Lodoto, G., Williams, J.P., 2022. Demographics of young stars and their protoplanetary disks: lessons learned on disk evolution and its connection to planet formation. In: Inutsuka, S.I., Aikawa, Y., Muto, T., Tomida, K., Tamura, M. (Eds.), *Protostars and Planets VII*. University of Arizona Press, Arizona arXiv.
- Marocchi, Y., Longeau, A., Goupil, R.L., Dijon, D., Pinto, G., Neukampf, J., Villeneuve, J., Jaquet, E., 2024. Isotopic evolution of the inner solar system revealed by size-dependent oxygen isotopic variation in chondrules. *Geochim. Cosmochim. Acta*. 371, 52–64.
- McKeegan, K.D., Kallio, A.P.A., Heber, V.S., Jarzebinski, G., Mao, P.H., Coath, C.D., Kunihiro, T., Wiens, R.C., Nordholt, J.E., Moses Jr, R.W., Reisenfeld, D.B., Jurewicz, A.J.G., Burnett, D.S., 2011. The oxygen isotopic composition of the Sun inferred from captured solar wind. *Science* 332, 1528–1532.
- Mendybaev, R.A., Kamibayashi, M., Teng, F.Z., Savage, P.S., Georg, R.B., Richter, F.M., Tachibana, S., 2021. Experiments quantifying elemental and isotopic fractionations during evaporation of CAI-like melts in low-pressure hydrogen and in vacuum: Constraints on thermal processing of CAIs in the protoplanetary disk. *Geochim. Cosmochim. Acta*. 292, 557–576.
- Morizet, Y., Paris, M., Gaillard, F., Scaillet, B., 2010. C-O-H fluid solubility in haplobasalt under reducing conditions: An experimental study. *Chem. Geol.* 279, 1–16.
- Nuth, J.A., Brearley, A.J., Scott, E.R.D., 2005. Microcrystals and amorphous materials in comets and primitive meteorites: Keys to understanding processes in the early Solar System, in: Krot, A.N., Scott, E.R.D., Reipurth, B. (Eds.), *Workshop on Chondrites and the Protoplanetary disk*. *Astronomical Society of the Pacific Conference Series*, vol. 341, pp. 675–700.
- Pascucci, I., Tachibana, S., 2010. In: *Protoplanetary Dust: Astrophysical and Cosmochemical Perspectives*. Cambridge Univ. Press, New York, p. 263.
- Pawley, A.R., Holloway, J.R., McMillan, P.F., 1992. The effect of oxygen fugacity on the solubility of carbon-oxygen fluids in basaltic melt. *Earth Planet Sci. Lett.* 110, 213–225.
- Pontoppidan, K.M., Brearley, A.J., 2010. Dust particle size evolution. In: Apai, D., Lauretta, D.S. (Eds.), *Protoplanetary Dust: Astrophysical and Cosmochemical Perspectives*. Cambridge University Press, New York, pp. 191–229.
- Ramananjeyulu, P.S., Chandra, K., Kulkarni, A.S., Yadav, C.S., Saha, A., Saxena, M.K., Tomar, B.S., Ramakumar, K.L., 2014. Determination of total gas content and its composition in Indian PFBR blanket pellets. *J. Radioanal. Nucl. Chem.* 301, 117–124.
- Ritger, P.L., Peppas, N.A., 1987. A simple equation for description of solute release I. Fickian ad non-fickian release from non-swellable devices in the form of slabs, spheres, cylinders of discs. *J. Control. Release*. 5, 23–36.
- Sakamoto, N., Seto, Y., Itoh, S., Kuramoto, K., Fujino, K., Nagashima, K., Krot, A.N., Yurimoto, H., 2007. Remnants of the early solar system water enriched in heavy oxygen isotopes. *Science* 317, 231–233.
- Sano, T., Inutsuka, S.I., Turner, N.J., Stome, J.M., 2004. Angular momentum transport by magnetohydrodynamic turbulence in accretion disks: Gas pressure dependence of the saturation level of the magnetorotational instability. *Astrophys. J.* 605, 321–339.
- Schroeder, I.R.H.G., Altwegg, K., Balsiger, H., Berthelier, J.J., Keyser, J.D., Fiethe, B., Gasc, S., Gombosi, T., Rubin, M., Sémon, T., Tzou, C.Y., Wampller, S.F., Wurzel, P., 2019. $^{16}\text{O}/^{18}\text{O}$ ratio in water in the coma of comet 67P/Churyumov-Gerasimenko measured with the Rosetta/ROSINA double-focusing mass spectrometer. *Astron. Astrophys.* 630, A29.
- Seto, Y., Sakamoto, N., Fujino, K., Kaito, T., Okikawa, T., Yurimoto, H., 2008. Mineralogical characterization of a unique material having heavy oxygen isotope anomaly in matrix of the primitive carbonaceous chondrite Acfer 094. *Geochim. Cosmochim. Acta*. 72, 2723–2734.
- Signorile, M., Zamirri, L., Tsuchiyama, A., Ugliengo, P., Bonino, F., Marta, G., 2020. On the surface acid-base properties of amorphous and crystalline Mg_2SiO_4 as probed by adsorbed CO , CO_2 , and CD_3CN . *ACS Earth Space Chem.* 4, 345–354.
- Smith, R.L., Pontoppidan, K.M., Young, E.D., Morris, M.R., van Dishoeck, E.F., 2009. High-precision C^{17}O , C^{18}O , and C^{16}O measurements in young stellar objects: Analogues for CO self-shielding in the early solar system. *Astrophys. J.* 701, 163–175.
- Takigawa, A., Tachibana, S., Nagahara, H., Ozawa, K., Yokoyama, M., 2009. Anisotropic evaporation of forsterite and its implication for dust formation conditions in circumstellar environments. *Astrophys. J.* 707, L97–L101.
- Wood, J.A., Morfill, G.E., 1988. A review of solar nebula models. In: Kerridge, J.F., Matthews, M.S. (Eds.), *Meteorites and the Early Solar System*. University of Arizona Press, Arizona, pp. 329–347.
- Yamamoto, D., Tachibana, S., 2018. Water vapor pressure dependence of crystallization kinetics of amorphous forsterite. *ACS Earth Space Chem.* 2, 778–786.
- Yamamoto, D., Kuroda, M., Tachibana, S., Sakamoto, N., Yurimoto, H., 2018. Oxygen isotope exchange between amorphous silicate and water vapor and its implications for oxygen isotope evolution in the early Solar System. *Astrophys. J.* 865, 98.
- Yamamoto, D., Tachibana, S., Kawasaki, N., Yurimoto, H., 2020. Survivability of presolar isotopic signatures of amorphous silicate dust in the protosolar disk. *Meteoritic. Planet. Sci.* 55, 1281–1292.
- Yamamoto, D., Kawasaki, N., Tachibana, S., Kamibayashi, M., Yurimoto, H., 2021. An experimental study on oxygen isotope exchange reaction between CAI melt and low-pressure water vapor under simulated Solar nebula conditions. *Geochim. Cosmochim. Acta*. 314, 108–120.
- Yamamoto, D., Kawasaki, N., Tachibana, S., Kamibayashi, M., Yurimoto, H., 2022. Oxygen isotope exchange kinetics between CAI melt and carbon monoxide gas: Implication for CAI formation in the earliest solar system. *Geochim. Cosmochim. Acta*. 336, 104–112.
- Yoshioka, T., Nakashima, D., Nakamura, T., Shcheka, S., Keppler, H., 2019. Carbon solubility in silicate melts in equilibrium with a CO-CO_2 gas phase and graphite. *Geochim. Cosmochim. Acta*. 259, 129–143.
- Yurimoto, H., Krot, A.N., Choi, B.G., Aléon, J., Kunihiro, T., Brearley, A.J., 2008. Oxygen isotopes of chondritic components, in: MacPherson, G.J. (Eds.), *Reviews in Mineralogy & Geochemistry*. *Mineralogical Society of America* 68, pp. 141–186.
- Yurimoto, H., Kuramoto, K., 2004. Molecular cloud origin for the oxygen isotope heterogeneity in the Solar System. *Science* 305, 1763–1766.
- Yurimoto, H., Nagasawa, H., Mori, Y., Matsubayashi, O., 1994. Micro-distribution of oxygen isotopes in a refractory inclusion from the Allende meteorite. *Earth Planet Sci. Lett.* 128, 47–53.